Measurement of the differential cross section $d\sigma/dt$ in elastic $p\bar{p}$ scattering at $\sqrt{s} = 1.96$ TeV

V. M. Abazov,[33] B. Abbott,[71] B. S. Acharya,[27] M. Adams,[47] T. Adams,[45] G. D. Alexeev,[33] G. Alkhazov,[37] A. Alton,[59,*] G. Alverson,[58] G. A. Alves,[1] M. Aoki,[46] A. Askew,[45] S. Atkins,[56] K. Augsten,[8] C. Avila,[6] F. Badaud,[11] L. Bagby,[46] B. Baldin,[46] D. V. Bandurin,[45] S. Banerjee,[27] E. Barberis,[58] P. Baringer,[54] J. Barreto,[2] J. F. Bartlett,[46] U. Bassler,[16] V. Bazterra,[47] A. Bean,[54] M. Begalli,[2] L. Bellantoni,[46] S. B. Beri,[25] G. Bernardi,[15] R. Bernhard,[20] I. Bertram,[40] M. Besançon,[16] R. Beuselinck,[41] V. A. Bezzubov,[36] P. C. Bhat,[46] S. Bhatia,[61] V. Bhatnagar,[25] G. Blazey,[48] S. Blessing,[45] K. Bloom,[62] A. Boehnlein,[46] D. Boline,[68] E. E. Boos,[35] G. Borissov,[40] T. Bose,[57] A. Brandt,[74] O. Brandt,[21] R. Brock,[60] G. Brooijmans,[66] A. Bross,[46] D. Brown,[15] J. Brown,[15] X. B. Bu,[46] M. Buehler,[46] V. Buescher,[22] V. Bunichev,[35] S. Burdin,[40,†] C. P. Buszello,[39] E. Camacho-Pérez,[30] W. Carvalho,[2] B. C. K. Casey,[46] H. Castilla-Valdez,[30] S. Caughron,[60] S. Chakrabarti,[68] D. Chakraborty,[48] K. M. Chan,[52] A. Chandra,[76] E. Chapon,[16] G. Chen,[54] S. Chevalier-Théry,[16] D. K. Cho,[73] S. W. Cho,[29] S. Choi,[29] B. Choudhary,[26] S. Cihangir,[46] D. Claes,[62] J. Clutter,[54] M. Cooke,[46] W. E. Cooper,[46] M. Corcoran,[76] F. Couderc,[16] M.-C. Cousinou,[13] A. Croc,[16] D. Cutts,[73] A. Das,[43] G. Davies,[41] S. J. de Jong,[31,32] E. De La Cruz-Burelo,[30] C. De Oliveira Martins,[2] F. Déliot,[16] R. Demina,[67] D. Denisov,[46] S. P. Denisov,[36] S. Desai,[46] C. Deterre,[16] K. DeVaughan,[62] H. T. Diehl,[46] M. Diesburg,[46] P. F. Ding,[42] A. Dominguez,[62] A. Dubey,[26] L. V. Dudko,[35] D. Duggan,[63] A. Duperrin,[13] S. Dutt,[25] A. Dyshkant,[48] M. Eads,[62] D. Edmunds,[60] J. Ellison,[44] V. D. Elvira,[46] Y. Enari,[15] H. Evans,[50] A. Evdokimov,[69] V. N. Evdokimov,[36] G. Facini,[58] L. Feng,[48] T. Ferbel,[67] F. Fiedler,[22] F. Filthaut,[31,32] W. Fisher,[60] H. E. Fisk,[46] M. Fortner,[48] H. Fox,[40] S. Fuess,[46] A. Garcia-Bellido,[67] J. A. García-González,[30] G. A. García-Guerra,[30,‡] V. Gavrilov,[34] P. Gay,[11] W. Geng,[13,60] D. Gerbaudo,[64] C. E. Gerber,[47] Y. Gershtein,[63] G. Ginther,[46,67] G. Golovanov,[33] A. Goussiou,[78] P. D. Grannis,[68] S. Greder,[17] H. Greenlee,[46] E. M. Gregores,[3] G. Grenier,[18] Ph. Gris,[11] J.-F. Grivaz,[14] A. Grohsjean,[16,§] S. Grünendahl,[46] M. W. Grünewald,[28] T. Guillemin,[14] G. Gutierrez,[46] P. Gutierrez,[71] A. Haas,[66,∥] S. Hagopian,[45] J. Haley,[58] L. Han,[5] K. Harder,[42] A. Harel,[67] J. M. Hauptman,[53] J. Hays,[41] T. Head,[42] T. Hebbeker,[19] D. Hedin,[48] H. Hegab,[72] A. P. Heinson,[44] U. Heintz,[73] C. Hensel,[21] I. Heredia-De La Cruz,[30] K. Herner,[59] G. Hesketh,[42,¶] M. D. Hildreth,[52] R. Hirosky,[77] T. Hoang,[45] J. D. Hobbs,[68] B. Hoeneisen,[10] M. Hohlfeld,[22] I. Howley,[74] Z. Hubacek,[8,16] V. Hynek,[8] I. Iashvili,[65] Y. Ilchenko,[75] R. Illingworth,[46] A. S. Ito,[46] S. Jabeen,[73] M. Jaffré,[14] A. Jayasinghe,[71] R. Jesik,[41] K. Johns,[43] E. Johnson,[60] M. Johnson,[46] A. Jonckheere,[46] P. Jonsson,[41] J. Joshi,[44] A. W. Jung,[46] A. Juste,[38] K. Kaadze,[55] E. Kajfasz,[13] D. Karmanov,[35] P. A. Kasper,[46] I. Katsanos,[62] R. Kehoe,[75] S. Kermiche,[13] N. Khalatyan,[46] A. Khanov,[72] A. Kharchilava,[65] Y. N. Kharzheev,[33] I. Kiselevich,[34] J. M. Kohli,[25] A. V. Kozelov,[36] J. Kraus,[61] S. Kulikov,[36] A. Kumar,[65] A. Kupco,[9] T. Kurča,[18] V. A. Kuzmin,[35] S. Lammers,[50] G. Landsberg,[73] P. Lebrun,[18] H. S. Lee,[29] S. W. Lee,[53] W. M. Lee,[46] J. Lellouch,[15] H. Li,[12] L. Li,[44] Q. Z. Li,[46] J. K. Lim,[29] D. Lincoln,[46] J. Linnemann,[60] V. V. Lipaev,[36] R. Lipton,[46] H. Liu,[75] Y. Liu,[5] A. Lobodenko,[37] M. Lokajicek,[9] R. Lopes de Sa,[68] H. J. Lubatti,[78] R. Luna-Garcia,[30,**] A. L. Lyon,[46] A. K. A. Maciel,[1] R. Madar,[16] R. Magaña-Villalba,[30] S. Malik,[62] V. L. Malyshev,[33] Y. Maravin,[55] J. Martínez-Ortega,[30] R. McCarthy,[68] C. L. McGivern,[54] M. M. Meijer,[31,32] A. Melnitchouk,[61] L. Mendoza,[6] D. Menezes,[48] P. G. Mercadante,[3] M. Merkin,[35] A. Meyer,[19] J. Meyer,[21] F. Miconi,[17] J. Molina,[2,††] N. K. Mondal,[27] H. da Motta,[1] M. Mulhearn,[77] L. Mundim,[2] E. Nagy,[13] M. Naimuddin,[26] M. Narain,[73] R. Nayyar,[43] H. A. Neal,[59] J. P. Negret,[6] P. Neustroev,[37] S. F. Novaes,[4] T. Nunnemann,[23] G. Obrant,[37,∥∥] V. Oguri,[2] J. Orduna,[76] N. Osman,[13] J. Osta,[52] M. Padilla,[44] A. Pal,[74] N. Parashar,[51] V. Parihar,[73] S. K. Park,[29] R. Partridge,[73,∥] N. Parua,[50] A. Patwa,[69] B. Penning,[46] M. Perfilov,[35] Y. Peters,[42] K. Petridis,[42] G. Petrillo,[67] P. Pétroff,[14] M.-A. Pleier,[69] P. L. M. Podesta-Lerma,[30,‡‡] V. M. Podstavkov,[46] M.-E. Pol,[1] A. V. Popov,[36] W. L. Prado da Silva,[2] M. Prewitt,[76] D. Price,[50] N. Prokopenko,[36] J. Qian,[59] A. Quadt,[21] B. Quinn,[61] M. S. Rangel,[1] K. Ranjan,[26] P. N. Ratoff,[40] I. Razumov,[36] P. Renkel,[75] I. Ripp-Baudot,[17] F. Rizatdinova,[72] M. Rominsky,[46] A. Ross,[40] C. Royon,[16] P. Rubinov,[46] R. Ruchti,[52] G. Sajot,[12] P. Salcido,[48] A. Sánchez-Hernández,[30] M. P. Sanders,[23] B. Sanghi,[46] A. Santoro,[2] A. S. Santos,[4] G. Savage,[46] L. Sawyer,[56] T. Scanlon,[41] R. D. Schamberger,[68] Y. Scheglov,[37] H. Schellman,[49] S. Schlobohm,[78] C. Schwanenberger,[42] R. Schwienhorst,[60] J. Sekaric,[54] H. Severini,[71] E. Shabalina,[21] V. Shary,[16] S. Shaw,[60] A. A. Shchukin,[36] R. K. Shivpuri,[26] V. Simak,[8] P. Skubic,[71] P. Slattery,[67] D. Smirnov,[52] K. J. Smith,[65] G. R. Snow,[62] J. Snow,[70] S. Snyder,[69] S. Söldner-Rembold,[42] L. Sonnenschein,[19] K. Soustruznik,[7] J. Stark,[12] D. A. Stoyanova,[36] M. A. Strang,[74,§§] M. Strauss,[71] L. Stutte,[46] L. Suter,[42] P. Svoisky,[71] M. Takahashi,[42] M. Titov,[16] V. V. Tokmenin,[33] Y.-T. Tsai,[67] K. Tschann-Grimm,[68] D. Tsybychev,[68] B. Tuchming,[16] C. Tully,[64] L. Uvarov,[37] S. Uvarov,[37] S. Uzunyan,[48] R. Van Kooten,[50] W. M. van Leeuwen,[31] N. Varelas,[47] E. W. Varnes,[43] I. A. Vasilyev,[36] P. Verdier,[18] A. Y. Verkheev,[33] L. S. Vertogradov,[33] M. Verzocchi,[46] M. Vesterinen,[42] D. Vilanova,[16] P. Vokac,[8] H. D. Wahl,[45] M. H. L. S. Wang,[46] J. Warchol,[52] G. Watts,[78] M. Wayne,[52] J. Weichert,[22]

L. Welty-Rieger,[49] A. White,[74] D. Wicke,[24] M. R. J. Williams,[40] G. W. Wilson,[54] M. Wobisch,[56] D. R. Wood,[58] T. R. Wyatt,[42] Y. Xie,[46] R. Yamada,[46] W.-C. Yang,[42] T. Yasuda,[46] Y. A. Yatsunenko,[33] W. Ye,[68] Z. Ye,[46] H. Yin,[46] K. Yip,[69] S. W. Youn,[46] J. Zennamo,[65] T. Zhao,[78] T. G. Zhao,[42] B. Zhou,[59] J. Zhu,[59] M. Zielinski,[67] D. Zieminska,[50] and L. Zivkovic[73]

(The D0 Collaboration)

[1]*LAFEX, Centro Brasileiro de Pesquisas Físicas, Rio de Janeiro, Brazil*
[2]*Universidade do Estado do Rio de Janeiro, Rio de Janeiro, Brazil*
[3]*Universidade Federal do ABC, Santo André, Brazil*
[4]*Universidade Estadual Paulista, São Paulo, Brazil*
[5]*University of Science and Technology of China, Hefei, People's Republic of China*
[6]*Universidad de los Andes, Bogotá, Colombia*
[7]*Charles University, Faculty of Mathematics and Physics, Center for Particle Physics, Prague, Czech Republic*
[8]*Czech Technical University in Prague, Prague, Czech Republic*
[9]*Center for Particle Physics, Institute of Physics, Academy of Sciences of the Czech Republic, Prague, Czech Republic*
[10]*Universidad San Francisco de Quito, Quito, Ecuador*
[11]*LPC, Université Blaise Pascal, CNRS/IN2P3, Clermont, France*
[12]*LPSC, Université Joseph Fourier Grenoble 1, CNRS/IN2P3, Institut National Polytechnique de Grenoble, Grenoble, France*
[13]*CPPM, Aix-Marseille Université, CNRS/IN2P3, Marseille, France*
[14]*LAL, USA, Université Paris-Sud, CNRS/IN2P3, Orsay, France*
[15]*LPNHE, Universités Paris VI and VII, CNRS/IN2P3, Paris, France*
[16]*CEA, Irfu, SPP, Saclay, France*
[17]*IPHC, Université de Strasbourg, CNRS/IN2P3, Strasbourg, France*
[18]*IPNL, Université Lyon 1, CNRS/IN2P3, Villeurbanne, France and Université de Lyon, Lyon, France*
[19]*III. Physikalisches Institut A, RWTH Aachen University, Aachen, Germany*
[20]*Physikalisches Institut, Universität Freiburg, Freiburg, Germany*
[21]*II. Physikalisches Institut, Georg-August-Universität Göttingen, Göttingen, Germany*
[22]*Institut für Physik, Universität Mainz, Mainz, Germany*
[23]*Ludwig-Maximilians-Universität München, München, Germany*
[24]*Fachbereich Physik, Bergische Universität Wuppertal, Wuppertal, Germany*
[25]*Panjab University, Chandigarh, India*
[26]*Delhi University, Delhi, India*
[27]*Tata Institute of Fundamental Research, Mumbai, India*
[28]*University College Dublin, Dublin, Ireland*
[29]*Korea Detector Laboratory, Korea University, Seoul, Korea*
[30]*CINVESTAV, Mexico City, Mexico*
[31]*Nikhef, Science Park, Amsterdam, Netherlands*
[32]*Radboud University Nijmegen, Nijmegen, Netherlands*
[33]*Joint Institute for Nuclear Research, Dubna, Russia*
[34]*Institute for Theoretical and Experimental Physics, Moscow, Russia*
[35]*Moscow State University, Moscow, Russia*
[36]*Institute for High Energy Physics, Protvino, Russia*
[37]*Petersburg Nuclear Physics Institute, St. Petersburg, Russia*
[38]*Institució Catalana de Recerca i Estudis Avançats (ICREA) and Institut de Física d'Altes Energies (IFAE), Barcelona, Spain*
[39]*Uppsala University, Uppsala, Sweden*
[40]*Lancaster University, Lancaster LA1 4YB, United Kingdom*
[41]*Imperial College London, London SW7 2AZ, United Kingdom*
[42]*The University of Manchester, Manchester M13 9PL, United Kingdom*
[43]*University of Arizona, Tucson, Arizona 85721, USA*
[44]*University of California Riverside, Riverside, California 92521, USA*
[45]*Florida State University, Tallahassee, Florida 32306, USA*
[46]*Fermi National Accelerator Laboratory, Batavia, Illinois 60510, USA*
[47]*University of Illinois at Chicago, Chicago, Illinois 60607, USA*
[48]*Northern Illinois University, DeKalb, Illinois 60115, USA*
[49]*Northwestern University, Evanston, Illinois 60208, USA*
[50]*Indiana University, Bloomington, Indiana 47405, USA*
[51]*Purdue University Calumet, Hammond, Indiana 46323, USA*
[52]*University of Notre Dame, Notre Dame, Indiana 46556, USA*

^{53}*Iowa State University, Ames, Iowa 50011, USA*
^{54}*University of Kansas, Lawrence, Kansas 66045, USA*
^{55}*Kansas State University, Manhattan, Kansas 66506, USA*
^{56}*Louisiana Tech University, Ruston, Louisiana 71272, USA*
^{57}*Boston University, Boston, Massachusetts 02215, USA*
^{58}*Northeastern University, Boston, Massachusetts 02115, USA*
^{59}*University of Michigan, Ann Arbor, Michigan 48109, USA*
^{60}*Michigan State University, East Lansing, Michigan 48824, USA*
^{61}*University of Mississippi, University, Mississippi 38677, USA*
^{62}*University of Nebraska, Lincoln, Nebraska 68588, USA*
^{63}*Rutgers University, Piscataway, New Jersey 08855, USA*
^{64}*Princeton University, Princeton, New Jersey 08544, USA*
^{65}*State University of New York, Buffalo, New York 14260, USA*
^{66}*Columbia University, New York, New York 10027, USA*
^{67}*University of Rochester, Rochester, New York 14627, USA*
^{68}*State University of New York, Stony Brook, New York 11794, USA*
^{69}*Brookhaven National Laboratory, Upton, New York 11973, USA*
^{70}*Langston University, Langston, Oklahoma 73050, USA*
^{71}*University of Oklahoma, Norman, Oklahoma 73019, USA*
^{72}*Oklahoma State University, Stillwater, Oklahoma 74078, USA*
^{73}*Brown University, Providence, Rhode Island 02912, USA*
^{74}*University of Texas, Arlington, Texas 76019, USA*
^{75}*Southern Methodist University, Dallas, Texas 75275, USA*
^{76}*Rice University, Houston, Texas 77005, USA*
^{77}*University of Virginia, Charlottesville, Virginia 22901, USA*
^{78}*University of Washington, Seattle, Washington 98195, USA*

We present a measurement of the elastic differential cross section $d\sigma(p\bar{p} \to p\bar{p})/dt$ as a function of the four-momentum-transfer squared t. The data sample corresponds to an integrated luminosity of ≈ 31 nb^{-1} collected with the D0 detector using dedicated Tevatron $p\bar{p}$ Collider operating conditions at $\sqrt{s} = 1.96$ TeV and covers the range $0.26 < |t| < 1.2$ GeV^2. For $|t| < 0.6$ GeV^2, $d\sigma/dt$ is described by an exponential function of the form $Ae^{-b|t|}$ with a slope parameter $b = 16.86 \pm 0.10(\text{stat}) \pm 0.20(\text{syst})$ GeV^{-2}. A change in slope is observed at $|t| \approx 0.6$ GeV^2, followed by a more gradual $|t|$ dependence with increasing values of $|t|$.

I. INTRODUCTION

The differential cross section, $d\sigma/dt$, for $p\bar{p} \to p\bar{p}$, where t is the four-momentum-transfer squared [1], contains information about proton structure and nonperturbative aspects of $p\bar{p}$ interactions. In the $|t|$ range studied here, the nuclear scattering amplitude is expected to dominate

[2], and with increasing $|t|$, $d\sigma/dt$ is expected to fall exponentially followed by a local diffractive minimum, after which $d\sigma/dt$ will continue to decrease [3].

Studies of $d\sigma/dt$ at different center-of-mass energies, $\sqrt{s}$, have demonstrated an effect known as shrinkage, namely, that the slope of the exponential falloff of the differential cross section as a function of $|t|$ becomes larger with increasing $\sqrt{s}$, and the $|t|$ value at which the local diffraction minimum occurs is reduced [4]. It has also been observed that the shape of the local diffractive minimum is different between pp and $p\bar{p}$ elastic scattering [5]. The elastic differential cross section plays an important role in constraining soft diffractive models [6–8] which cannot be directly calculated by perturbative QCD [9].

In this article, we present a measurement of the $p\bar{p}$ elastic differential cross section at $\sqrt{s} = 1.96$ TeV in the range $0.26 < |t| < 1.2$ GeV^2, measured using the forward proton detector (FPD) spectrometer system of the D0 experiment [10]. Since p and $\bar{p}$ elastic scattering angles are typically very small (on the order of milliradians), they are

*with visitor from Augustana College, Sioux Falls, SD, USA
†with visitor from The University of Liverpool, Liverpool, UK
‡with visitor from UPIITA-IPN, Mexico City, Mexico
§with visitor from DESY, Hamburg, Germany
$^{\|}$with visitor from SLAC, Menlo Park, CA, USA
¶with visitor from University College London, London, UK
**with visitor from Centro de Investigacion en Computacion-IPN, Mexico City, Mexico
††with visitor from Universidad Nacional de Asuncion, Facultad de Ingenieria, Asuncion, Paraguay
‡‡with visitor from ECFM, Universidad Autonoma de Sinaloa, Culiacán, Mexico
§§with visitor from Ohio State University, Columbus, OH, USA
$^{\|\|}$Deceased

not covered by the main D0 detector. The elastically scattered protons and antiprotons are tagged with detectors inserted in the beam pipe on either side of the interaction point (IP). Our measurement extends the $|t|$ range previously studied by the CDF ($0.025 < |t| < 0.29$ GeV^2) [11] and by the E710 ($0.034 < |t| < 0.65$ GeV^2) [12] Collaborations at the Tevatron and constitutes the first confirmation of a change in the $|t|$ dependence of $d\sigma(p\bar{p} \rightarrow p\bar{p})/dt$ at center-of-mass energy $\sqrt{s} = 1.96$ TeV. A similar measurement in pp collisions at $\sqrt{s} = 7.0$ TeV has recently been reported by the TOTEM Collaboration [13] showing similar trends for the slope of the differential cross section and for the position of the local diffraction minimum, although the local minimum found in pp elastic scattering is much more pronounced than the kink we observe.

This article is organized as follows. First we describe, in Sec. II, the D0 detector, with particular emphasis on the FPD. Next, in Sec. III, we discuss various aspects of the selection of the sample of candidate elastic scattering events, including the details on the position measurements in the FPD, their alignment, the reconstruction of p and $\bar{p}$ scattering angles, the background subtraction, the measurements of acceptance and efficiencies. Systematic uncertainties are discussed in Sec. IV and the results of this measurement are described in Sec. V.

II. D0 DETECTOR

We briefly describe the elements of the detector that are relevant for the measurement reported here. A detailed description of the D0 detector can be found in Ref. [10]. The central tracking system of the D0 detector comprises a silicon microstrip tracker and a central fiber tracker, surrounded by a 2 T superconducting solenoidal magnet. The pseudorapidity [14] coverage for the tracking detectors is $|\eta| < 3$ for the silicon microstrip tracker and $|\eta| < 2.5$ for the central fiber tracker. Outside of the superconducting magnet, the liquid-argon and uranium calorimeter are composed of three sections housed in separate cryostats:

a central calorimeter section covering the pseudorapidity range $|\eta| < 1.1$ and two end calorimeter sections that extend coverage to $|\eta| \approx 4.2$ [15]. A muon system [16], outside of the calorimetry, consists of three layers of tracking detectors and scintillation trigger counters, and large toroidal magnets for muon momentum measurement. The luminosity monitor (LM) consists of plastic scintillator arrays located at $z = \pm 140$ cm (where z is measured from the IP along the nominal direction of the proton beam), and covers the pseudorapidity range $2.7 < |\eta| < 4.4$. The LM is used to detect nondiffractive inelastic collisions and to make an accurate determination of the luminosity.

A. Forward proton detectors

Figure 1 shows the layout of the main components of the FPD system relevant to this measurement [10]. In the center of the diagram is the interaction point, IP, at the center of the main D0 detector. A scattered proton/antiproton goes through three Tevatron quadrupole magnets (with a field gradient of about 20 T/m) which alternate defocusing in the horizontal and vertical planes, passes through the first station of detectors, goes through a region free from magnetic field where electrostatic separators are located, and arrives at a second station of detectors.

The FPD consists of four quadrupole spectrometers on both the scattered proton (P) and scattered antiproton (A) sides plus a dipole spectrometer (not shown). Each quadrupole spectrometer is composed of two scintillating fiber detectors, one located at about 23 m (A_1 or P_1) and the second at about 31 m (A_2 or P_2) from the IP along the Tevatron beam line. Both detectors are either above (U), below (D), on the inner side (I), or on the outer side (O) of the beam line. Given the location of the two detectors, the spectrometers on the A side are named A_U, A_D, A_I, and A_O (a similar definition is made for the P side). The pseudorapidity range covered by the detectors is about $7.3 < |\eta| < 8.6$. Only the quadrupole spectrometers are used in this analysis, since the dipole spectrometer does not have any significant acceptance for elastically scattered antiprotons.
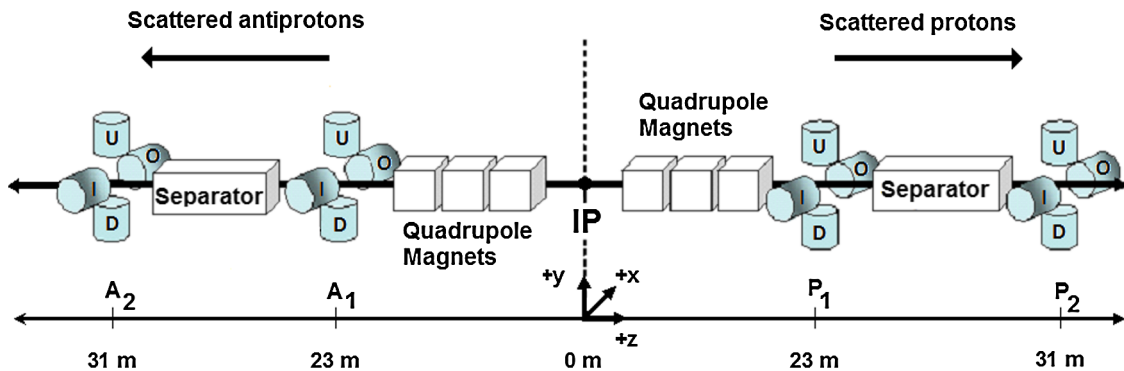

FIG. 1 (color online). Schematic view of the Roman pot stations (A_1, A_2, P_1, P_2) comprising the forward proton detector as described in the text (not drawn to scale). The dipole spectrometer is not shown. The letters U, D, I, O make reference to the up, down, inner, and outer detectors, respectively.
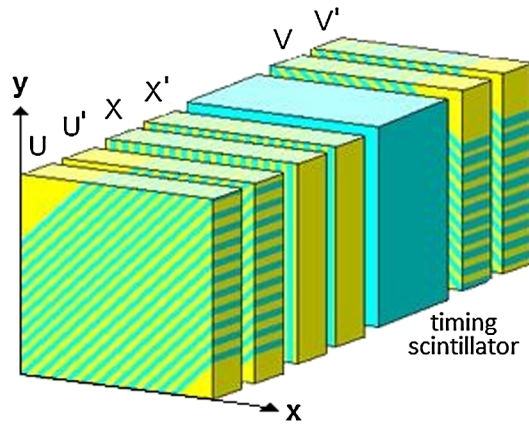
FIG. 2 (color online). Schematic view of the design of one FPD scintillating fiber detector. U, U′, V, V′, X, and X′ are the scintillating fiber layers. The local detector x, y coordinates are indicated by the arrows. The scintillating fibers are indicated by the green stripes.

Scattered protons and antiprotons cross thin stainless steel windows at the entrance and exit of a vessel (Roman pot) containing the detectors [17]. The pots are remotely controlled and moved to within a few millimeters of the beam during stable beam conditions. The Roman pots house position detectors using 0.8 mm × 0.8 mm square double-clad polystyrene scintillating fibers to detect the passage of charged particles. Each position detector consists of six layers of scintillating fibers (U, U′, V, V′, X, X′), where the scintillating fibers of the U, U′ (V, V′) layers are rotated by plus (minus) 45 degrees with respect to the vertical X, X′ fibers (see Fig. 2).

The fibers of the "primed" planes are offset by 0.53 mm (two-thirds of a fiber width) with respect to the fibers of the "unprimed" layers. By combining the fiber information from primed and "unprimed" layers, we obtain "wide" fiber segments (about 1.07 mm wide) that are used for triggering and "fine" fiber segments (about 0.27 mm wide) used for offline hit reconstruction (see Fig. 3).
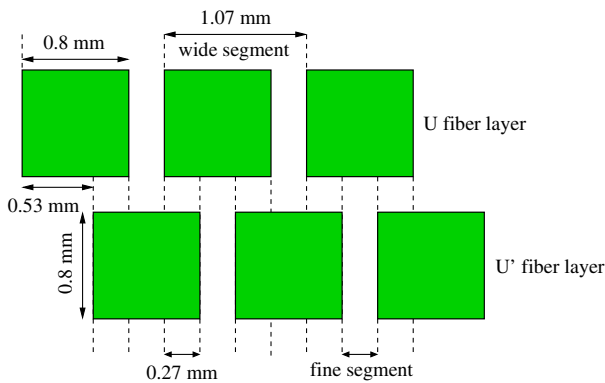

FIG. 3 (color online). Schematic view of part of the U and U′ fiber layers with the definitions of wide and fine fiber segments. Similar definitions are used for the X, X′ and V, V′ fiber layers.

Each detector also contains a scintillator (read out by a time-to-digital converter system [10]) which provides a time measurement for particles passing through the detector with a resolution of about 1 ns. The time measurement is used to distinguish particles coming from the center of the D0 detector from background beam halo particles (particles traveling far enough outside of the main beam core that they pass through the FPD detector).

Beyond the active areas of the detectors, matching square clear fibers transport signals from the scintillators to 16-channel multianode photomultiplier tubes. The electronic signals are subsequently amplified, shaped, and sent to the D0 triggering and data acquisition system [10].

The elastic triggers are defined by the presence of coincident hits in all four detectors in one of the four possible configurations of a $\bar{p}$ spectrometer and a diagonally opposite (collinear) p spectrometer: $A_U P_D$, $A_D P_U$, $A_I P_O$, and $A_O P_I$. Several different conditions on the hits in the scintillating fiber detectors were used in the triggers: a tight (T) trigger that registered a single hit formed by the coincidence of UU′, VV′, XX′ wide segments; a medium (M) trigger that allowed up to three wide segments; and a loose (L) trigger that allowed hits formed from coincidences of two out of the three UU′, VV′, XX′ wide segments with no requirements on number of hits. To reduce backgrounds from inelastic collisions, LM vetoes (no hits in either the LM counters on the proton and antiproton sides) were included as part of the elastic triggers. The timing scintillator in each detector is only used for providing time information for off-line analysis and is not part of the triggers.

III. ELASTIC EVENT SELECTION

An initial data sample is obtained by requiring events to satisfy one of the elastic triggers. The p and $\bar{p}$ hit coordinates are measured in the FPD system using the fibers' information and then used to select the sample of elastic scattering events. We align the detectors with respect to the beam and then use the beam transport matrices [18] (which are functions of the currents of the magnets located between the IP and the FPD detectors and correlate the x, y coordinates and scattering angle of a particle at two specific z locations) to reconstruct the paths of protons and antiprotons through this region of the Tevatron. Next, background subtraction and efficiency corrections are performed. We use a Monte Carlo (MC) event generator to apply corrections for acceptance, detector resolution, beam divergence, and IP size effects.

A. Data Sample

The data for this analysis were collected with dedicated beam conditions designed to facilitate the positioning of the FPD Roman pots as close to the beam axis as possible. The Tevatron injection tune with the betatron function of $\beta^* = 1.6$ m at the D0 IP was used instead of the standard

$\beta^* = 0.35$ m lattice [19]. Additionally, only one proton bunch and one antiproton bunch were present in the Tevatron. Scraping in the vertical and horizontal planes to remove the halo tails of the bunches was performed and the electrostatic separators were turned off before initiating collisions. The initial instantaneous luminosity was about 0.5×10^{30} cm^{-2} s^{-1} with a lifetime of about 30 hours, corresponding to a mean number of ≈ 0.8 interactions per bunch crossing. The recorded luminosity is about $\mathcal{L} = 31$ nb^{-1}, which corresponds to the sum of two data sets used in this analysis, each with different detector positions with respect to the beams. One set of data was taken with the closest detector position reaching about 4 mm with respect to the beam (data set 1), and the other data set was taken with detectors about 1 mm closer to the beam (data set 2). For the given instantaneous luminosity and the conditions of this store, about 33% of the elastic events are expected to be produced together with an inelastic collision in the same bunch crossing.

Approximately 20×10^6 events were recorded using a special trigger list optimized for diffractive physics, including triggers for elastic, single diffractive, and double pomeron [20] exchange. This analysis uses elastic triggers, which make up about 10% of the total data collected. Independent triggers were used to determine efficiencies.

B. Hit reconstruction

We reconstruct the proton and antiproton hits using fibers with an associated signal above the same threshold as used in the FPD trigger system, that is tuned to accept hits from a minimum ionizing particle. For each fiber in an unprimed layer above threshold, we verify if there is an adjacent fiber in the primed layer in order to define a fine fiber segment through which the particle traversed the plane. Events with more than four fibers firing in a plane are typically not due to single particles and are rejected (more than 99% of the elastic triggered events survive this condition). We require at least two out of the three UU′, VV′, and XX′ fine segments to be reconstructed in each detector, with their intersection yielding the transverse coordinates of the hit. Since noise in some of the fibers could produce fake hits, in the case of more than one reconstructed hit in a detector (which happens in about 10% of the events), we weight the hits by the sum of the analog-to-digital converter pulse height of all the fibers that contributed to each hit and retain only the hit with the highest weight. The correction for the selection efficiency, discussed in Sec. III I, accounts for elastic events discarded by this requirement.

Utilizing events with fine segments in U, V, and X, we are able to estimate the offset in position and resolution within each detector by taking the difference between the x coordinate obtained from UV fiber intersection and a similar measurement using the X fiber plane. Most of the detectors used in this analysis have a resolution of about

150 μm with the exception of some of the A2 detectors that had several inactive scintillating fibers, degrading their resolution to about 250 μm.

C. Selection of candidate elastic events

Elastic collisions produce one of the four possible hit configurations in the FPD: $A_U P_D$, $A_D P_U$, $A_I P_O$, $A_O P_I$. Since the inner and outer detectors are farther from the beam than the U and D detectors, they have poorer acceptance for elastic events and are only used for alignment purposes (see Sec. III D). If we compare the hit coordinates reconstructed by each of the two detectors of one spectrometer, we observe a correlation band from particles going through the spectrometer, but also observe some uncorrelated background hits (see Fig. 4). We require hits to lie within $\pm 3\sigma$ ($\sigma \approx 220$ μm) from the center of the band. We determine the quantity σ by fitting a Gaussian distribution obtained by projecting the hits onto an axis perpendicular to the correlation band.

We then investigate the correlation between the coordinates of the protons and antiprotons in diagonally opposite
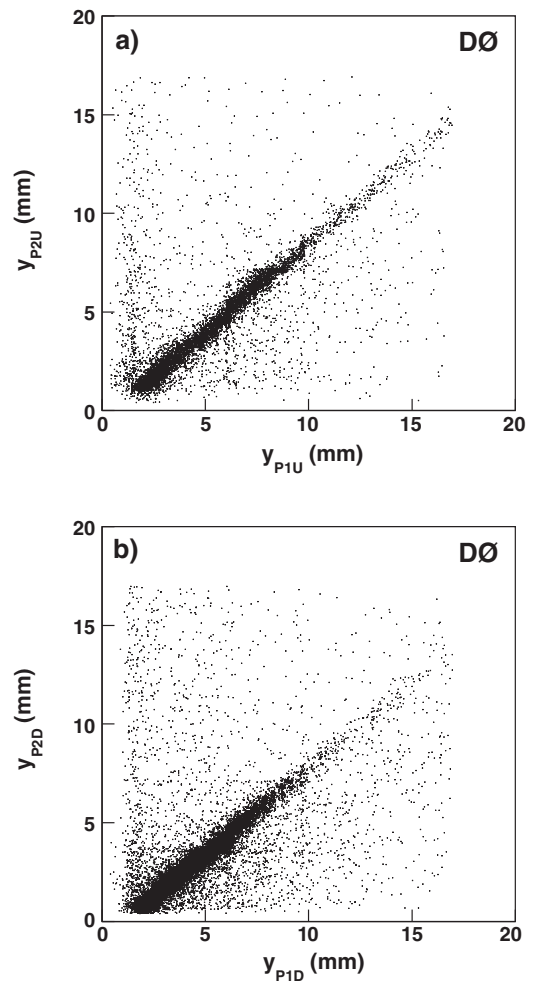
FIG. 4. Comparison of detector y coordinates in the spectrometers (a) P_U and (b) P_D.

spectrometers. In addition to the expected correlation due to the collinearity of elastic events, some background contamination due to halo particles remains. This contribution is reduced through the use of the FPD timing system, but there is still some residual background, partially due to inefficiency of the trigger scintillators and to different acceptances of the spectrometers. A correction for the contribution from halo within the correlation band is discussed in Sec. III F.

For a specific set of p and $\bar{p}$ spectrometers in an elastic combination, we observe that elastic events with a proton passing through a small region of the detectors in one spectrometer will have $\bar{p}$ positions distributed over a similar but somewhat larger region of the diagonally opposite spectrometer. Depending on the location of the proton, the Gaussian distribution of the $\bar{p}$ position may be truncated due to the finite detector size. After calculating the $\bar{p}$ acceptance correction as a function of the coordinates of the proton spectrometer, a fiducial cut is applied in the P_1 detectors such that only regions in these detectors which require a correction of 2% or less are used. The region we select in the P_1 detectors is thus guaranteed to correspond to an acceptance greater than 98% in the other three detectors. Figure 5 shows the y_p vs $y_{\bar{p}}$ coordinate correlation plots (y coordinate measured in the local coordinate system shown in Fig. 6), the tagging of the hits according to time-of-flight information, and the fiducial cuts applied

(indicated by the dashed lines). We also check that there is no activity in the calorimeter for events in the elastic data sample. The contribution to the elastic sample from events that have a nonzero energy in the calorimeter is less than 0.1% of the total number of selected events. Most of the elastic events produced in beam crossings with multiple $p\bar{p}$ interactions are suppressed by the vetoes on the LM detectors.

D. Forward proton detector alignment

In order to reconstruct the tracks from the protons and antiprotons, we first align the detectors with respect to the beam and then determine the position and angle of a particle at the IP from the measured hit positions in the FPD detectors after application of the Tevatron transport matrices.

The location of the detectors with respect to the beam is determined using a sample of tracks that pass through one vertical and one horizontal detector at the same Roman pot station, allowing determination of the relative alignment of the detectors. We use elastic events to align one horizontal detector that did not have any overlap with the other detectors at the same z location. We define the center of a vertical and a horizontal pot at each Roman pot station and then measure the positions of all four detectors with respect to this reference system. Because of the beam optics the x (y) hit coordinate distributions in the vertical
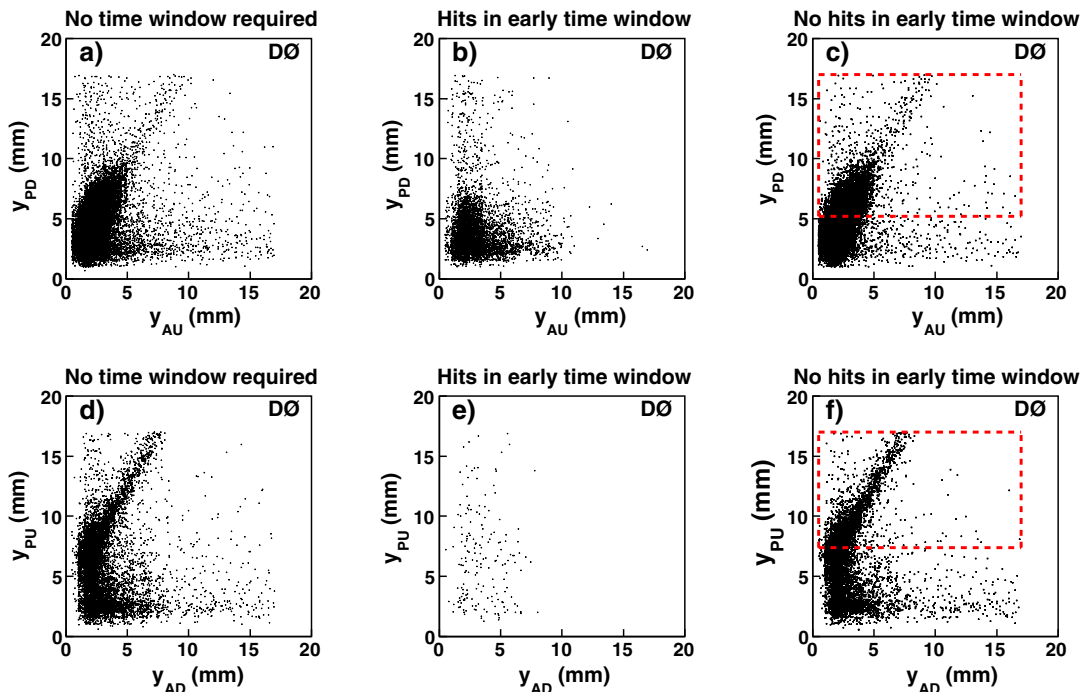

FIG. 5 (color online).   The correlation plots y_p vs $y_{\bar{p}}$ for the first detectors in the spectrometers (y coordinates measured in the local coordinate system shown in Fig. 6) for A_UP_D and A_DP_U. Plots (a) and (d) show the correlations without any timing requirement; (b) and (e) correspond to hits with a coincident tag in the corresponding scintillator early time windows; (c) and (f) show events with no hits within the early time window (most of the hits in this case are in the in-time window). The dashed lines correspond to the fiducial requirements applied.
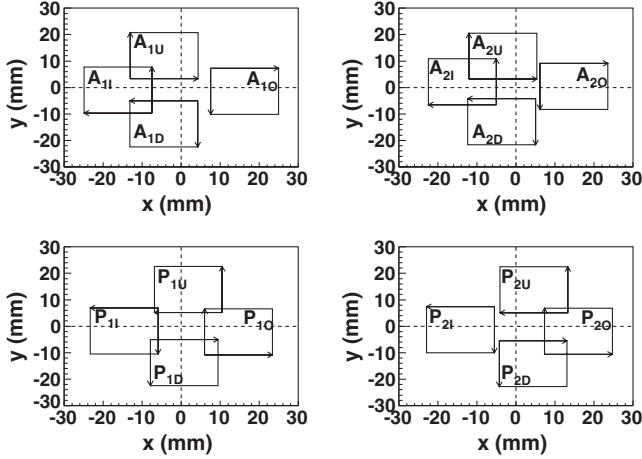
FIG. 6. Detector positions with respect to beam center (dashed lines) for the data set corresponding to the closest pot insertion to the beam. The arrows indicate the local coordinate system in each detector.
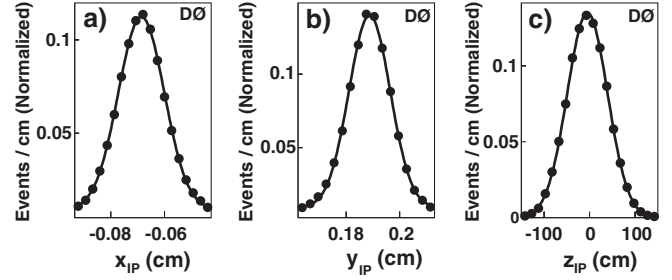

FIG. 7. Size of the IP determined by the reconstruction of the primary vertex from nonelastic triggers (black points) fitted with a Gaussian function (solid line). (a) x distribution of the IP. (b) y distribution of the IP. (c) z distribution of the IP.

proton (horizontal antiproton) detectors are narrower than in the vertical antiproton (horizontal proton) detectors. Because of this effect, the offset of the beam in x for the vertical proton detectors (and the offset of the beam in y for the horizontal antiproton detectors) is determined by fitting a Gaussian distribution to the x and y distributions in these detectors. All other beam offsets are obtained given the fact that the reconstructed IP offset and scattering angle is the same for both the proton and antiproton in an elastic event. We take the average over all four elastic combinations to determine the offset of the beam at each Roman pot station. Figure 6 shows the position of each detector obtained with the alignment procedure described above for the data set corresponding to the detector configuration with Roman pots located closest to the beam. The coordinates are plotted with respect to the beam coordinate system (dashed lines shown in the figure). For the data collected with the Roman pots retracted farther away from the beam line, we use positional difference information obtained from the pot motion system added to the previously determined aligned positions. The uncertainty of the location of the detectors after the alignment procedure is estimated to be about 200 μm.

E. Reconstruction of $p/\bar{p}$ tracks and $|t|$ measurement

The Tevatron transport matrices are unique for these data due to the use of the injection lattice. The beam radius (at 1σ level) ranges from 0.4 mm to 0.8 mm at the different FPD detector locations while the beam divergence is about 44 μrad. The change in the proton or antiproton divergence caused by the quadrupoles system is typically of the order of 1 mrad for the smallest $|t|$ values considered in this measurement.

The size of the IP in x, y, and z is typically determined by reconstructing the primary vertex using the tracking

detectors [10]. Given the absence of central tracks in elastic events, data from nonelastic triggers, simultaneously collected with the elastic scattering events used in this analysis, are used to obtain the x, y, and z distributions of the IP. The size of the IP in each direction is obtained by fitting a Gaussian function to each distribution. The measured Gaussian width of the IP distribution is about 100 μm in the transverse plane and about 45 cm along the z axis (see Fig. 7). The offsets observed in x and y from the primary vertex reconstruction are due to the fact that the center of the tracker is shifted with respect to the beam line. We use the reconstructed elastic events to determine these offsets, as described below.

To tag an elastic event, we reconstruct the coordinates of the hits in the two proton and two antiproton detectors. The difference of coordinates between a proton and antiproton detector yields a Gaussian distribution with a width related to the fiber offset and resolution of the two detectors, the IP size, and the beam divergence. Given the previously estimated detector resolutions and IP size, these distributions can be used to estimate the beam divergence. The values obtained are similar (40 ± 5 μrad) to those estimated using the injection tune lattice parameters. With the coordinates of the two detectors in each spectrometer we determine the offsets of the IP (x_0, y_0) and the horizontal and vertical scattering angles (θ_x, θ_y respectively) by using the following equations:

$$ x_i = M_{x,i}x_0 + L_{x,i}\theta_x \qquad y_i = M_{y,i}y_0 + L_{y,i}\theta_y \quad (1) $$

where x_i, y_i are the hit coordinates in a detector i and $M_{x,i}$, $L_{x,i}$ ($M_{y,i}$, $L_{y,i}$) are the transport matrix elements in the horizontal (vertical) axis for that detector location. We verify that the distributions of the difference of the IP offsets and scattering angles obtained from the proton spectrometer and the antiproton spectrometer for every event are centered around zero. Since the values of θ obtained are of the order of milliradians, the four-momentum-transfer squared, t, can be approximated as

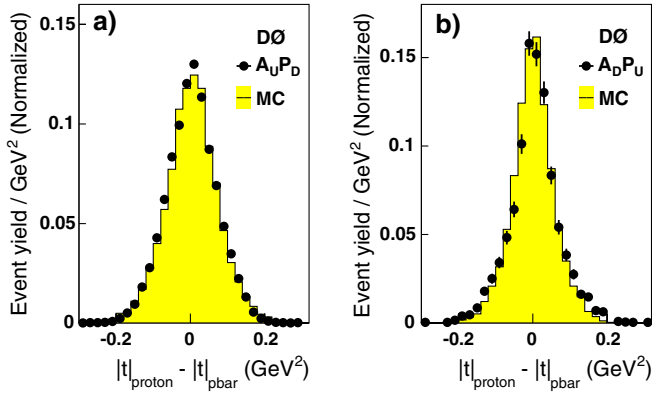$$ t = -p^2(\theta_x^2 + \theta_y^2) \quad (2) $$

FIG. 8 (color online). Difference in the reconstructed $|t|$ between p and $\bar{p}$ vertical spectrometers. The MC (solid line) expected distribution is compared to data (solid points). (a) $A_U P_D$ combination. (b) $A_D P_U$ combination. The number of entries in each distribution is normalized to unity.

where p is the momentum of the scattered particle. Given that the momenta of the elastically scattered proton and antiproton are the same as that of the incoming particles (980 GeV) and that the beam momentum spread is negligibly small (0.014%) [21], the uncertainty in $|t|$ is dominated by the measurement uncertainty of the scattering angle. Figure 8 shows the difference in the reconstructed $|t|$ from the $\bar{p}$ and p vertical spectrometers, $\Delta|t| = |t|_{\bar{p}} - |t|_p$. The nonzero standard deviation of $\Delta|t|$, $\sigma_{\Delta t}$, is due to the resolution on $|t|_p$ and $|t|_{\bar{p}}$. The average of $|t|_p$ and $|t|_{\bar{p}}(|t|_{\text{ave}} = (|t|_p + |t|_{\bar{p}})/2)$ has a resolution of approximately $\sigma_{\Delta|t|}/2$. The $|t|$ bin size is chosen as the largest of the observed $\sigma_{\Delta|t|}$ for the two detector combinations $A_U P_D$ and $A_D P_U$, where the difference in $\sigma_{\Delta|t|}$ results from different detector resolutions. We also study the $|t|$ resolution as a function of $|t|$ and observe a gradual increase with $|t|$, from 0.02 GeV^2 to 0.04 GeV^2, which is reflected in the bin widths.

F. Background Subtraction

The primary source of background in the selected sample is due to beam halo, consisting of either a halo proton and a halo antiproton in the same bunch crossing or a halo particle combined with a single diffractive event. A halo particle passing through the proton detectors in the time window for the protons which have undergone elastic scattering usually passes through the diagonally opposite antiproton detector at an earlier time (and vice versa). Therefore, the time information can be used to veto events with early time hits, consistent with halo protons and antiprotons in the elastic sample. The veto is not 100% efficient due to a combination of scintillator efficiency and positioning of the detectors with respect to the beam (a closer detector position both increases a detector's signal acceptance and its ability to reject halo). Consequently, it is necessary to subtract the remaining background.

We consider an event to be caused by $\bar{p}$ (p) halo if one or both of the two p ($\bar{p}$) detectors of an elastic combination have hits in their early time interval. We require events to have no activity in either the $\bar{p}_{\text{halo}}$ or the p_{halo} timing window. We select background samples by requiring hits consistent with p halo and $\bar{p}$ halo simultaneously. First, we verify that outside the elastic correlation band between the coordinates of a proton and antiproton detector the signal tagged events have the same $|t|$ dependence as the background tagged ones (see Fig. 5). Next, assuming that signal and background tagged events also have the same $|t|$ dependence inside the correlation band, we use the ratio of these two distributions and use it to estimate the percentage of background events inside the signal tagged correlation band. This background is subtracted from all events inside the correlation band to obtain dN/dt as a function of $|t|$. The amount of background subtracted inside the elastic correlation band varies from 1% at low $|t|$ to 5% at high $|t|$. The absolute uncertainty of the background, which is propagated as a statistical uncertainty to $d\sigma/dt$, varies from 0.3% at low $|t|$ to 5.0% at high $|t|$. As a cross check, we vary the detector band cuts from 3.0σ to 3.5σ and to 6.0σ, to allow more background, and obtain similar dN/dt results after applying the same background subtraction procedure (within 1%).

G. Monte Carlo simulation of elastic events

We have developed a MC generator interfaced with the Tevatron transport matrices to generate elastic events. The MC allows us to study the geometrical acceptance of the detectors, resolution of the position measurement, alignment, and effects of the beam size and beam divergence at the IP. The generation of events is based on an Ansatz function that we obtain by fitting the dN/dt distribution of the data. We study the acceptance and bin migration effects using samples generated with a wide range of different dN/dt Ansatz distributions. The variations in the corrections are included as systematic uncertainties.

The positions of hits in each detector are transformed into fiber hit information, and the reconstruction then proceeds using these hits, following the same procedure as with the data. The reconstructed correlation patterns in MC are in good agreement with those observed in data. In addition, the MC also predicts the widths of the different correlations as shown in Figs. 8 and 9.

H. Acceptance and bin migration correction

Because of accelerator optics, protons and antiprotons of a particular $|t|$ are transported to an elliptical region in the x–y plane at each detector location. Each detector has a different coverage in the azimuthal angle ϕ and therefore a different coverage of the ellipses of constant $|t|$. The ϕ acceptance correction accounts for the fraction of the $|t|$ ellipse for each $|t|$ bin that is not covered by the fiducial area used in each detector. This correction depends only on
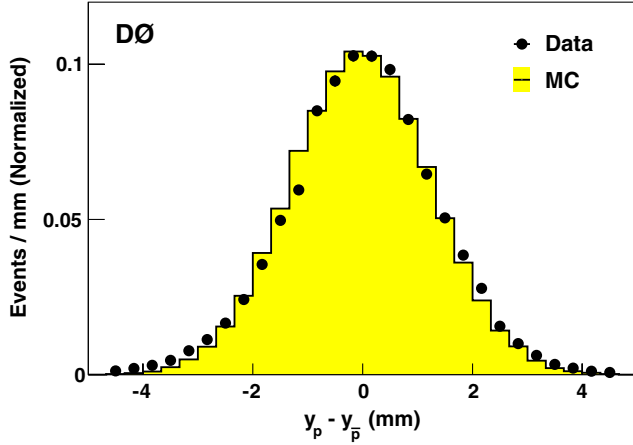
FIG. 9 (color online).   Comparison of MC (solid line) and data (black points) for the coordinate difference y_p-$y_{\bar{p}}$ for the elastic configuration $A_{1,U}P_1D$ for the data set with detectors closer to the beam.

the detector location with respect to the particle beam and on the geometry of the fiducial area used in the detector for selecting the events. Figure 10 shows the ϕ acceptance calculated as a function of $|t|$ for data at the closest detector position with respect to the beam and after the fiducial cuts. We obtain similar results for the ϕ acceptance using the MC described in the previous section before adding the effects of beam divergence, IP size, and detector resolution. The uncertainty in the ϕ acceptance correction, which comes from the size of the MC sample used, is less than 0.1% at low $|t|$ values and less than 1.0% at high $|t|$ values. To estimate the correction for bin migration effects that is applied in data to obtain the $d\sigma/dt$ distribution, we include the measured values of beam divergence, IP size, detector resolution, and pot position uncertainties in the MC
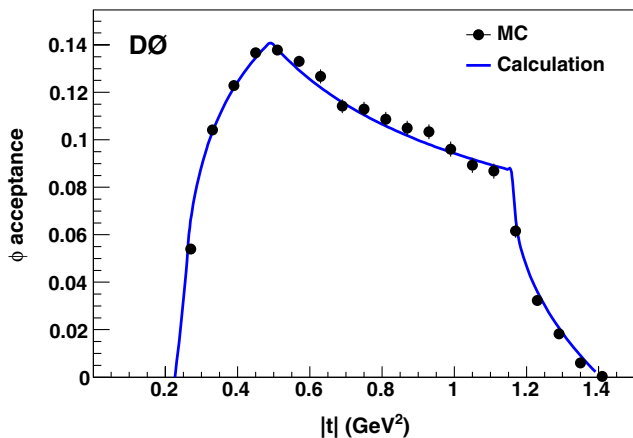

FIG. 10 (color online).   Azimuthal acceptance of the FPD in data, after fiducial cuts, for the closest detector position of the A_UP_D elastic combination. The points correspond to MC, the solid line corresponds to the calculation of the ϕ acceptance from the detector positions and the fiducial area.

generator and compare to a same size MC sample with no smearing effects.

I. Selection and trigger efficiencies

We simultaneously determine the effects of selection and trigger efficiencies for each of the four detectors corresponding to an elastic configuration. To determine the efficiency of a particular detector, we use an independent trigger which does not include that detector. We obtain the dN/dt distributions with an elastic track reconstructed in the other three detectors and for all four detectors, with the trigger conditions satisfied. The ratio of the two distributions is used to extract the efficiency of the detector as a function of $|t|$ (where $|t|$ is reconstructed from the coordinates of the opposite side spectrometer). To avoid any additional effect from detector acceptance, we use only hits in the other three detectors in a region determined to have full geometrical acceptance in the detector of interest. We repeat a similar procedure for each of the four detectors in every elastic combination and multiply the efficiencies of the four detectors to determine the final efficiency correction. Typical selection and trigger efficiencies are in the range of 50% to 70% depending on the detector and trigger requirements. Additionally, we make a correction for the veto in the LM which was part of the elastic trigger. This veto filters out elastic events that are produced in coincidence with an inelastic collision in the same bunch crossing (pileup). To make this correction, we use a trigger based on hits in the proton spectrometers with no LM requirement and determine the fraction of candidate elastic events reconstructed in coincidence with the LM. We find that about 27% (20%) of elastic events for data set 1 (2) as defined in Sec. III A were removed by the LM veto.

J. Luminosity

Since elastic data were collected with Tevatron conditions modified with respect to standard operations of the D0 experiment, we compare the number of inclusive jet events obtained from our data to the number of jet events used for the inclusive cross section measurement discussed in [22] to determine the integrated luminosity. The corresponding integrated luminosity for data set 1 (2) is 18.3 nb^{-1} (12.6 nb^{-1}), with an uncertainty of 13%. We add in quadrature the uncertainty in the standard luminosity determination (6.1% [23]) and obtain an overall normalization uncertainty of 14.4%.

IV. SYSTEMATIC UNCERTAINTIES

The major $|t|$-dependent contributions to the systematic uncertainties in the measurement of $d\sigma/dt$ are due to detector efficiencies, beam divergence, detector positions, and the choice of the Ansatz function. The luminosity measurement contributes to the overall normalization

uncertainty. The Tevatron beam transport matrices are known with high precision (within 0.1%) and therefore produce a small uncertainty in our results compared to the other sources. We take the uncertainty in the position of the pot from the beam center as an extra "smearing" factor for the hit coordinates in the MC. Since the efficiencies vary with $|t|$, we fit either a polynomial or an exponential function to each trigger efficiency and propagate the uncertainties in the fit parameters to $d\sigma/dt$, using the covariance matrix of the fit. For the beam divergence term, we vary the beam divergence by ± 5 μrad in the MC, and we propagate the change in the acceptance correction bin-by-bin to $d\sigma/dt$. We also consider 26 possible variations of the Ansatz function used in the MC to account for the uncertainties in the logarithmic slopes before and after the kink and also for the $|t|$ value where the kink is observed.

V. RESULTS

In total, we have four independent measurements of $d\sigma/dt$ that come from the two elastic combinations (A_UP_D and A_DP_U) and two data sets, which agree with each other within the uncertainties. We combine the four measurements using a bin-by-bin weighted average. The resulting values for the $d\sigma/dt$ distribution, together with their total uncertainties, are listed in Table I and shown in Fig. 11. The uncertainties are the total experimental uncertainties excluding the 14.4% normalization uncertainty. The $|t|$ bin centers are determined using the prescription described in [24], however, the values found are very close to the middle of the bin. Two phenomenological model predictions for $\sqrt{s} = 1.96$ TeV (Bourrely *et al.* [25], Deile *et al.* [26]) are also shown. The model of

TABLE I. The $d\sigma/dt$ differential cross section. The statistical and systematic uncertainties are added in quadrature. The luminosity uncertainty of 14.4% is not included.

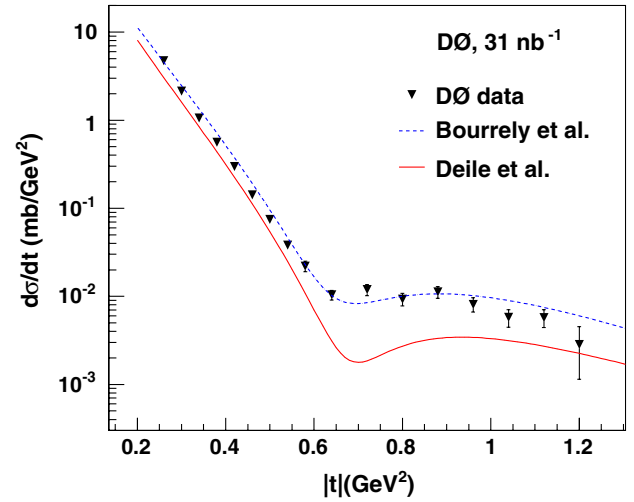| $|t|$ (GeV^2)	$d\sigma/d|t|$ (mb/GeV^2)
0.26	$(47.3 \pm 2.6) \times 10^{-1}$
0.30	$(21.4 \pm 0.72) \times 10^{-1}$
0.34	$(10.6 \pm 0.37) \times 10^{-1}$
0.38	$(5.64 \pm 0.22) \times 10^{-1}$
0.42	$(2.98 \pm 0.14) \times 10^{-1}$
0.46	$(14.2 \pm 0.83) \times 10^{-2}$
0.50	$(7.46 \pm 0.51) \times 10^{-2}$
0.54	$(3.81 \pm 0.36) \times 10^{-2}$
0.58	$(2.20 \pm 0.30) \times 10^{-2}$
0.64	$(1.04 \pm 0.13) \times 10^{-2}$
0.72	$(1.19 \pm 0.17) \times 10^{-2}$
0.80	$(9.28 \pm 1.5) \times 10^{-3}$
0.88	$(11.2 \pm 1.7) \times 10^{-3}$
0.96	$(8.11 \pm 1.5) \times 10^{-3}$
1.04	$(5.77 \pm 1.3) \times 10^{-3}$
1.12	$(5.73 \pm 1.3) \times 10^{-3}$
1.20	$(2.84 \pm 1.7) \times 10^{-3}$

FIG. 11 (color online). The measured $d\sigma/dt$ differential cross section. The normalization uncertainty of 14.4% is not shown. The uncertainties are obtained by adding in quadrature statistical and systematic uncertainties. The predictions of Bourrely *et al.* ([25]) and Deile *et al.* ([26]) are compared to the data.

Bourrely *et al.* shows a good description of the data in shape and normalization and is able to reproduce the kink within experimental uncertainties.

The $|t|$ range covered by our measurement is $0.26 < |t| < 1.2$ GeV^2. We observe a change in the logarithmic slope of the $d\sigma/dt$ distribution at $|t| \approx 0.6$ GeV^2. A fit to the $d\sigma/dt$ distribution in the range $0.26 < |t| < 0.6$ with an exponential function of the form $Ae^{-b|t|}$ yields a logarithmic slope parameter of $b = 16.86 \pm 0.10(\text{stat}) \pm 0.20(\text{syst})$ GeV^{-2} ($\chi^2 = 6.63$ for 7 degrees of freedom).
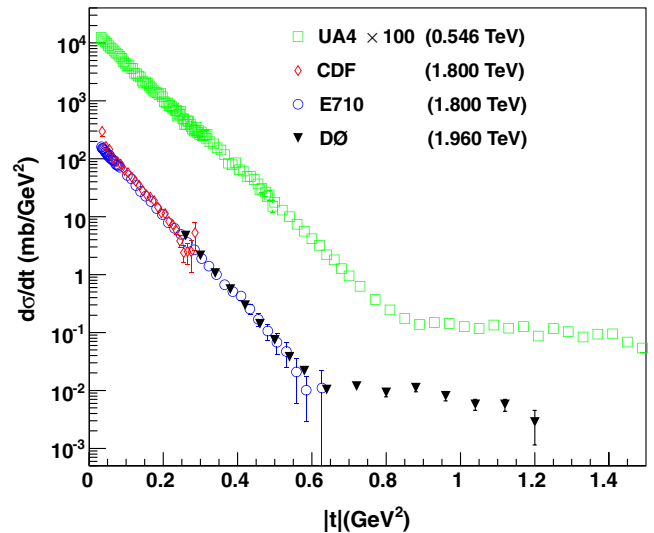

FIG. 12 (color online). The $d\sigma/dt$ differential cross section measured by the D0 Collaboration and compared to the CDF and E710 measurements at $\sqrt{s} = 1.8$ TeV, and to the UA4 measurement at $\sqrt{s} = 0.546$ TeV (scaled by a factor of 100). A normalization uncertainty of 14.4% on the D0 measurement is not shown.

Figure 12 shows a comparison of our results to those obtained at $\sqrt{s} = 1.8$ TeV by the CDF and E710 Tevatron Collaborations [11,12], and also to that of the UA4 Collaboration at $\sqrt{s} = 0.546$ TeV [27]. Our measurement of the slope parameter agrees within uncertainties with previous measurements by the CDF ($b = 16.98 \pm 0.25$ GeV^{-2}) and E710 ($b = 16.30 \pm 0.30$ GeV^{-2}) Collaborations. A comparison of the shape of our measured $d\sigma/dt$ to UA4 measurement shows that the kink in $d\sigma/dt$ moves towards lower $|t|$ values as the energy is increased, but, as in the UA4 data, we do not see a distinct minimum as observed in pp elastic interactions ([13]).

In summary, we have presented the first measurement of $d\sigma(p\bar{p} \to p\bar{p})/dt$ as a function of $|t|$ at $\sqrt{s} = 1.96$ TeV. Our measurement extends the $|t|$ and $\sqrt{s}$ range previously studied and shows a change in the $|t|$ dependence, consistent with the features expected for the transition between two diffractive regimes.

[1] $t = (p_f - p_i)^2$ where p_i and p_f are the initial and final particles four-momenta, respectively.
[2] M. Block, Phys. Rep. **436**, 71 (2006).
[3] G. Giacomelli, Phys. Rep. **23**, 123 (1976).
[4] G. Alberi and G. Goggi, Phys. Rep. **74**, 1 (1981).
[5] A. Breakstone *et al.*, Phys. Rev. Lett. **54**, 2180 (1985).
[6] E. Nagy *et al.* (CHHOV Collaboration), Nucl. Phys. **B150**, 221 (1979).
[7] V. Barone and E. Predazzi, *High Energy Particle Diffraction* (Springer-Verlag, Berlin, 2002).
[8] A. Donnachie and P. Landshoff, Phys. Lett. B **387**, 637 (1996).
[9] J. Forshaw and D. A. Ross, *Quantum Chromodynamics and The Pomeron* (Cambridge University Press, Cambridge, 1997).
[10] V. M. Abazov *et al.* (D0 Collaboration), Nucl. Instrum. Methods Phys. Res., Sect. A **565**, 463 (2006).
[11] F. Abe *et al.* (CDF Collaboration), Phys. Rev. D **50**, 5518 (1994).
[12] N. Amos *et al.* (E710 Collaboration), Phys. Lett. B **247**, 127 (1990).
[13] G. Antchev *et al.* (TOTEM Collaboration), Europhys. Lett. **95**, 41001 (2011).
[14] The pseudorapidity is defined as $\eta = -\ln[\tan(\theta/2)]$, where θ is the polar angle with respect to the proton beam direction.
[15] S. Abachi *et al.* (D0 Collaboration), Nucl. Instrum. Methods Phys. Res., Sect. A **338**, 185 (1994).
[16] V. M. Abazov *et al.* (D0 Collaboration), Nucl. Instrum. Methods Phys. Res., Sect. A **552**, 372 (2005).
[17] U. Amaldi *et al.*, Phys. Lett. B **44**, 112 (1973).
[18] M. G. Minty and F. Zimmerman, *Measurement and Control of Charged Particle Beams* (Springer-Verlag, Berlin, 2003).
[19] S. D. Holmes, FERMILAB, Report No. FERMILAB-TM-2484, 1998.
[20] V. M. Abazov *et al.* (D0 Collaboration), Phys. Lett. B **705**, 193 (2011).
[21] J. Stogin, T. Sen, and R. S. Moore, JINST **7**, T01001 (2012).
[22] V. M. Abazov *et al.* (D0 Collaboration), Phys. Rev. Lett. **101**, 062001 (2008).
[23] T. Andeen *et al.*, FERMILAB, Report No. FERMILAB-TM-2365, 2007.
[24] G. Laferty and T. Wyatt, Nucl. Instrum. Methods Phys. Res., Sect. A **355**, 541 (1995).
[25] C. Bourrely, J. Soffer, and T. T. Wu, Eur. J. Phys. C **28**, 97 (2003).
[26] M. Deile, *et al.*, arXiv:1002.3527v2.
[27] M. Bozzo *et al.* (UA4 Collaboration), Phys. Lett. B **155**, 197 (1985).